

Improving constraints on primordial non-Gaussianity from Quaia with a new cosmological observable: angular redshift fluctuations

J. R. Bermejo-Climent^{1, 2, 3, 4, *}, C. Hernández-Monteagudo^{1, 2}, A. Crespo-Pérez^{1, 2}, J. Martín Camalich^{1, 2}, D. Alonso⁵, G. Fabbian^{6, 7}, and K. Storey-Fisher⁸

¹ Instituto de Astrofísica de Canarias, C/ Vía Láctea, s/n, E-38205 La Laguna, Tenerife, Spain

² Departamento de Astrofísica, Universidad de La Laguna, Avenida Francisco Sánchez, s/n, E-38205 La Laguna, Tenerife, Spain

³ MTA–CSFK Lendület “Momentum” Large-Scale Structure (LSS) Research Group, Konkoly Thege Miklós út 15-17, H-1121 Budapest, Hungary

⁴ Konkoly Observatory, HUN-REN Research Centre for Astronomy and Earth Sciences, H-1121 Budapest, Hungary

⁵ Department of Physics, University of Oxford, Denys Wilkinson Building, Keble Road, Oxford OX1 3RH, United Kingdom

⁶ Université Paris-Saclay, CNRS, Institut d’Astrophysique Spatiale, 91405, Orsay, France

⁷ Kavli Institute for Cosmology Cambridge, Madingley Road, Cambridge CB3 0HA, UK

⁸ Kavli Institute for Particle Astrophysics and Cosmology, Stanford University, 452 Lomita Mall, Stanford, CA 94305, USA

Received XXX; accepted YYY

ABSTRACT

Context. Angular redshift fluctuations (ARF) are a new cosmological observable, recently proposed in the literature. It measures the 2D angular deviations of the average redshift of a given matter tracer under an input redshift shell. Since it depends on the galaxy bias, it can be used to constrain primordial non-Gaussianity through the scale-dependent bias effect.

Aims. We analyze a sample of quasars built upon the Gaia satellite and unWISE data, Quaia, to measure the local non-Gaussianity parameter f_{NL} . This sample is particularly suitable for measuring f_{NL} due to its large volume coverage.

Methods. We measure the ARF power spectra from the Quaia catalog and combine their information with the 2D (projected) galaxy density and their cross-correlation with the *Planck* PR4 CMB lensing maps to jointly constrain f_{NL} .

Results. Assuming the universality relation, we measure $f_{NL} = -3 \pm 14$ at 68% confidence level by combining Quaia quasar angular density and ARF with the CMB lensing. This result is the second tightest constraint on f_{NL} using LSS two-point statistics to date and the best measurement achieved using two-point projected summary statistics, improving by $\sim 25\%$ the previous measurement from Quaia. Our results motivate the inclusion of ARF as an additional cosmological observable in future 2D analysis of upcoming datasets from large surveys.

Key words. primordial non-Gaussianity – large-scale structure – CMB cross-correlations

1. Introduction

Cosmic inflation was proposed in the early 1980s (Guth 1981; Starobinsky 1980) as a theory for the very early universe. The inflation framework was initially formulated to solve problems associated with the Big Bang scenario such as the horizon, flatness, and magnetic monopole problems; however, inflation is also capable of explaining the formation of primordial density perturbations (Starobinsky 1982; Guth & Pi 1985; Bardeen et al. 1983). Inflation is defined as a phase of exponential expansion of the Universe, driven by a scalar field ϕ . Several models of inflation have been proposed in the literature (see, e.g. Langlois 2010; Vazquez Gonzalez et al. 2020 for reviews), such that the model of inflation and its predictions are defined by choosing the form of the potential $V(\phi)$. The simplest inflationary models predict Gaussian initial conditions, although alternative inflationary models predict different levels of non-Gaussianity in the primordial density perturbations (Chen 2010; Takahashi 2014). A particularly simple configuration of non-Gaussianity has been characterized in the literature with the f_{NL} non-Gaussianity parameter, such that detecting $f_{NL} \neq 0$ is a signature of having non-Gaussian initial conditions. In practice, the f_{NL} parameter

describes the amplitude of a quadratic non-Gaussian term in the expression for the primordial potential.

The tightest constraint on f_{NL} is currently achieved by the measurements from the CMB bispectrum. Using *Planck* 2018 data, a value $f_{NL} = -0.9 \pm 5.1$ at 68% confidence level was reported in Planck Collaboration et al. (2019). However, in Dalal et al. (2008) it was first noticed that local non-Gaussian initial conditions lead to a characteristic scale-dependent signature in the galaxy bias, following a $1/k^2$ scale-dependence in the ratio between the total matter to observed density of galaxies. During the last decade, many works have performed measurements from the large-scale structure using the scale-dependent bias effect (Ross et al. 2012; Hernández-Monteagudo et al. 2014; Castorina et al. 2019; Mueller et al. 2021; Cabass et al. 2022; D’Amico et al. 2023, among others). In the last years, some measurements from LSS using the scale-dependent galaxy bias have been achieved using the eBOSS DR16 quasars: $f_{NL} = -12 \pm 21$ in Mueller et al. (2021) and $-4 < f_{NL} < 27$ in Cagliari et al. (2024) were the limits obtained at 68% confidence level using different methodologies. This constraint was improved to $f_{NL} = -3.6^{+9.1}_{-9.0}$ using the 3D power spectrum of DESI DR1 galaxies and quasars (Chaussidon et al. 2025), and more recently, Chudaykin et al. (2025) claimed that the DESI DR1 constraint can be improved

* e-mail: jose.bermejo@csfk.org

to $\sigma(f_{\text{NL}}) \gtrsim 4$ by adding the LSS bispectrum. Measuring f_{NL} from LSS is often challenging because it requires a very accurate control of observational systematics that affect the largest scales clustering signal, where the scale-dependent bias effect due to f_{NL} arises (see e.g. [Rezaie et al. 2021, 2024](#) for detailed analyses of the impact of observational systematics in f_{NL} measurements from eBOSS and DESI data).

The most common observable used in the literature for measuring f_{NL} from LSS is the 3D galaxy power spectrum in Fourier space. However, in many cases a two-dimensional analysis in the harmonic space can be more convenient for many reasons. In particular, a 2D analysis in tomographic redshift bins can be equivalent to a 3D analysis under certain conditions (see e.g. [Asorey et al. 2012; Camera et al. 2018](#)) and does not require to assume any fiducial cosmology or to neglect the redshift evolution inside a given redshift bin. Further, the possibility of performing cross-correlations with other observables such as the CMB lensing, and the redshift uncertainties in photometric surveys, make the 2D power spectrum a standard tool for the analysis of photometric galaxy counts. In this direction, many recent works have performed measurements of f_{NL} using 2D angular power spectra of galaxies (e.g. [Rezaie et al. 2024](#)) and their cross-correlation with the CMB lensing; in particular, using the *Planck* PR4 CMB lensing in cross-correlation with the LRG ([Bermejo-Climent et al. 2025](#)) and the QSO ([Krolewski et al. 2024; Chiarenza et al. 2025](#)) from DESI data.

In addition, several works in the literature ([Hernández-Monteagudo et al. 2020a,b; Lima-Hernández et al. 2022](#)) proposed a new 2D observable called “angular redshift fluctuations” (hereafter ARF) that can be combined together with the galaxy density and CMB information to constrain cosmological parameters. ARF are a new observable that introduce the redshift as a 2D field and measure the deviations of the mean redshift of the galaxies in each direction of the sky with respect to the average redshift of the matter tracer sample under any given redshift shell. It has been shown that this observable can be useful to constrain cosmological parameters itself and in combination with the standard angular density fluctuations, from the point of view of theoretical forecasts ([Legrand et al. 2021](#)) and also with real data applications to measure the growth of structures and the nature of gravity ([Hernández-Monteagudo et al. 2020b; Hernández-Monteagudo et al. 2024](#)).

As theoretically discussed in [Hernández-Monteagudo et al. \(2020a\)](#), ARF are sensitive to the galaxy bias, and in consequence, this new observable can be used to measure the local primordial non-Gaussianity f_{NL} thanks to the scale-dependent bias effect introduced in [Dalal et al. \(2008\)](#). In this work, we intend to explore with real cosmological datasets the sensitivity of ARF to f_{NL} . For this purpose, we use the Quaia catalog ([Storey-Fisher et al. 2024](#)), a quasar (QSO) sample extracted from the Gaia satellite DR3 observations and unWISE infrared data ([Lang 2014](#)), and we also add the CMB lensing information from the *Planck* PR4 data release to perform a cross-correlation analysis. The Quaia catalog has been already used to constrain structure growth ([Alonso et al. 2023](#)), to measure the power spectrum turnover scale ([Alonso et al. 2025](#)) and the primordial non-Gaussianity parameter ([Fabbian et al. 2025](#)) using its cross-correlation with the *Planck* CMB lensing. Despite the low number density of QSO, it is a full sky catalog covering the largest volume covered by any QSO catalog, which makes it a suitable dataset for primordial non-Gaussianity measurements given that the f_{NL} arises at the largest scales. Our aim in this work is to extend the analysis by [Fabbian et al. \(2025\)](#) with the inclusion of ARF as cosmological observable, to quantify the potential im-

provement on the f_{NL} uncertainty that can be achieved by adding ARF to future analyses of upcoming LSS surveys such as DESI, Euclid, and LSST.

This paper is organized as follows: in Sec. 2 we describe the formalism related to the scale-dependent bias induced by a primordial local non-Gaussianity and the projected 2D observables that we include in our analysis; in Sec. 3 we describe the datasets used for this measurement; in Sec. 4 we detail the methodology for our analysis pipeline; in Sec. 5 we present our results and robustness tests on the f_{NL} measurement, and in Sec. 6 we summarize our conclusions.

2. Theory

In this section we first provide a description of the physical model that originates a scale-dependent galaxy bias due to a local primordial non-Gaussianity (PNG) and then describe the cosmological observables in the 2D harmonic space involved in our analysis.

2.1. Primordial non-Gaussianity and scale dependent bias

If we assume a type of non-Gaussianity that depends only on the local value of the potential, the parametrization of the primordial potential can be written as follows ([Komatsu & Spergel 2001](#))

$$\Phi = \phi + f_{\text{NL}}(\phi^2 - \langle \phi \rangle^2), \quad (1)$$

where f_{NL} is the parameter that describes the amplitude of the non-Gaussian quadratic term, and ϕ is a random Gaussian field.

We study f_{NL} through its impact on the scale-dependent galaxy bias, as first introduced in [Dalal et al. \(2008\); Matarrese & Verde \(2008\)](#). If we assume the so-called universality relation for the halo mass function ([Slosar et al. 2008](#)) the contribution to the galaxy bias is given by

$$\Delta b(k, z) = 2(b_g - p)f_{\text{NL}} \frac{\delta_{\text{crit}}}{\alpha(k)}, \quad (2)$$

where $\delta_{\text{crit}} = 1.686$ is the threshold overdensity for spherical collapse, b_g is the z -dependent galaxy bias, p is a parameter that characterizes the response of quasars to PNG and $\alpha(k)$ is the relation between potential and density field, such that $\delta(k) = \alpha(k)\Phi(k)$. The value of $\alpha(k)$ is given by

$$\alpha(k) = \frac{2k^2 T(k) D(z)}{3\Omega_m} \frac{c^2}{H_0^2} \frac{g(0)}{g(\infty)}, \quad (3)$$

where $T(k)$ is the transfer function, $D(z)$ is the growth factor (normalized to be 1 at $z = 0$), Ω_m the matter density, and $g \equiv D/a$, such that the factor $g(\infty)/g(0) \simeq 1.3$ accounts for the different normalizations of $D(z)$ in the CMB and LSS literature. This definition of f_{NL} is, therefore, the so-called ‘CMB convention’. Note that other authors ([Carbone et al. 2008; Afshordi & Tolley 2008; Grossi et al. 2009](#)) have adopted the use of the ‘LSS convention’, where the $g(\infty)/g(0)$ factor is absorbed into the definition of f_{NL} , such that $f_{\text{NL}}^{\text{LSS}} \simeq 1.3 f_{\text{NL}}^{\text{CMB}}$. Throughout this paper, we fix $p = 1$ as a baseline; however, many works based on dark-matter-only simulations (e.g. [Adame et al. 2024](#)) have found significant deviations from $p = 1$. In this direction, some works ([Barreira 2020, 2022](#)) have stressed that we can only constrain the product $b_\phi f_{\text{NL}}$ through the scale-dependent bias effect, where b_ϕ is a parameter typically defined as $b_\phi = 2\delta_{\text{crit}}(b_g - p)$, in order to account for the uncertainties on p .

2.2. Cosmological observables

Our cosmological observables are the angular auto and cross-correlation power spectra of three fields: the CMB lensing, the galaxy number counts and the ARF. The angular power spectrum can be calculated as

$$C_\ell^{XY} = 4\pi \int \frac{dk}{k} \mathcal{P}(k) I_\ell^X(k) I_\ell^Y(k) \quad (4)$$

where $\mathcal{P}(k) \equiv k^3 P(k)/(2\pi^2)$ is the dimensionless primordial power spectrum and $I_\ell^X(k)$ is the kernel of the field X .

The CMB lensing quantities can be defined from the lensing potential

$$\phi(\hat{\mathbf{n}}, \chi) = \frac{2}{c^2} \int_0^\chi d\chi' \frac{\chi - \chi'}{\chi\chi'} \Phi(\chi' \hat{\mathbf{n}}, \chi') \quad (5)$$

where $\Phi(\hat{\mathbf{n}}, \chi)$ is the gravitational potential and the comoving distance is given by

$$\chi(z) = \int_0^z \frac{c dz'}{H(z')} \quad (6)$$

By expanding the gravitational potential in Fourier space and using the plane-wave expansion, we define the CMB lensing potential kernel as

$$I_\ell^{\phi_{\text{CMB}}}(k) = 2 \left(\frac{3\Omega_m H_0^2}{2k^2 c^2} \right) \int \frac{d\chi}{(2\pi)^{3/2}} \frac{\chi_* - \chi}{\chi_* \chi} \frac{1}{a(\chi)} j_\ell(k\chi) \delta(k, \chi) \quad (7)$$

where Ω_m is the present-day matter density, H_0 is the Hubble constant, $\delta(k, \chi)$ is the synchronous gauge linear matter density perturbation, χ_* is the comoving distance at the surface of last scattering, and j_ℓ the spherical Bessel functions.

Finally, the convergence $\kappa = \nabla^2 \phi/2$ is expanded in spherical harmonics as

$$\kappa(\hat{\mathbf{n}}) = -\frac{1}{2} \sum_{\ell, m} \ell(\ell + 1) \phi_{\ell m} Y_\ell^m(\hat{\mathbf{n}}) \quad (8)$$

and we relate the two kernels by

$$I_\ell^\kappa(k) = \frac{\ell(\ell + 1)}{2} I_\ell^\phi(k) \quad (9)$$

The 2D integrated window function for the galaxy number counts is given by

$$I_\ell^g(k) = \int \frac{d\chi}{(2\pi)^{3/2}} W(\chi) \Delta_\ell(k, \chi) \quad (10)$$

where $\Delta_\ell(k, \chi)$ is the observed number counts and $W(\chi)$ is a window function given by the redshift distribution of galaxies. At first order, the most important contribution to $\Delta_\ell(k, \chi)$ is given by the synchronous gauge source counts Fourier transformed and expanded into multipoles, $\Delta_\ell^s(k, \chi)$. We assume that $\Delta_\ell^s(k, \chi)$ is related to the underlying matter density field through a scale and redshift dependent galaxy bias b_g as

$$\Delta_\ell^s(k, \chi) = b_g(k, \chi) \delta(k, \chi) j_\ell(k\chi) \quad (11)$$

where $b_g(k, \chi)$ is given by the sum of a linear bias, which is not scale dependent, plus the scale dependent contribution given by Eq. 2. We also consider non-linear contributions to the power spectrum using halofit (Takahashi et al. 2012). In this paper, we do not include corrections from General Relativity to

the galaxy number counts. According to Alonso et al. (2023) the measured magnification bias s of the Quaia catalog for the $G < 20.5$ magnitude limit cut is expected to be $s \sim 0.4$, and this is the value for which the lensing magnification contribution vanishes. The rest of the General Relativity corrections tend to have a smaller impact on the galaxy number counts and its cross-correlations (e.g. Bermejo-Climent et al. 2021) and, in particular, their effects are expected to be negligible for primordial non-Gaussianity measurements (Alonso et al. 2015; Guedezounme et al. 2025).

The ARF field is formally defined as in Hernández-Monteagudo et al. (2020a):

$$(\delta z)(\hat{\mathbf{n}}) = \frac{\sum_{j \in \hat{\mathbf{n}}} (z_j - \bar{z}) w_j}{\sum_{j \in \hat{\mathbf{n}}} w_j} \quad (12)$$

where the j index runs over the galaxies pointing to a given direction $\hat{\mathbf{n}}$, \bar{z} is the average redshift of galaxies under a user-defined redshift window W which can be arbitrary, but in many cases we adopt a Gaussian form for simplicity, with an associated weight for each galaxy given by

$$w_j \equiv \exp \left[-\frac{(z_{\text{obs}} - z_j)^2}{2\sigma_z^2} \right], \quad (13)$$

with z_{obs} and σ_z the central redshift and the width of the Gaussian window. In this particular case, we choose to adopt a very wide Gaussian window, which is equivalent to selecting galaxies under the survey's intrinsic quasar redshift distribution, so $w_j = 1$ in practice and \bar{z} is the average redshift of the sample. The definition of the ARF field in Eq. 12 can be noisy when the number of galaxies per pixel is low or even zero. In this study, for practical reasons related to the limited number of QSO per unit of observed area, we adopt a second definition of the ARF field as in Hernández-Monteagudo et al. (2020b):

$$(\delta z)(\hat{\mathbf{n}}) = \frac{\sum_{j \in \hat{\mathbf{n}}} (z_j - \bar{z}) w_j}{\langle \sum_{j \in \hat{\mathbf{n}}} w_j \rangle_{\hat{\mathbf{n}}}} \quad (14)$$

where in the denominator we have taken the ensemble average of the density over all the survey footprint. It can be shown that the definition in Eq. 12 is insensitive to multiplicative systematics, while both definitions are sensitive to additive systematics, assuming there is no redshift dependence of the systematics under the redshift window W .

In order to calculate the ARF field kernel I_ℓ^z , we follow the same formalism that for the galaxy number counts but replacing in Eq. 10 the window function W by a redshift fluctuations weighted window W :

$$W(z, \bar{z}) \equiv W(z)(z - \bar{z}), \quad (15)$$

as implemented in the modified version of the Boltzmann code CAMB (Challinor & Lewis 2011a,b) named ARFCAMB¹ (Lima-Hernández et al. 2022).

3. Datasets

In this section, we present the two main ingredients of our analysis: the Quaia QSO catalog, extracted from Gaia data, which contains approximately ~ 1.3 million QSO, and the *Planck* PR4 release of the CMB lensing maps.

¹ ARFCAMB can be accessed at <https://github.com/chmATiac/ARFCAMB>

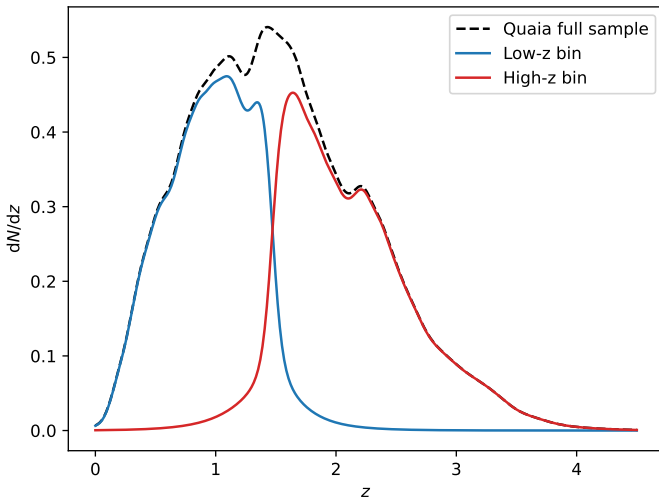


Fig. 1. Normalized redshift distribution of the Quaia QSO sample analyzed in this paper. The black dashed line corresponds to the full sample, while the blue and red lines correspond to the low and high redshift bins, respectively.

3.1. The Quaia QSO catalog

Quaia (Storey-Fisher et al. 2024) is a QSO catalog constructed from the Gaia DR3 quasar candidates sample and unWISE (Schlafly et al. 2019) infrared data. It is an all-sky catalog that covers the largest volume of any existing spectroscopic quasar sample. The full sample, with $G < 20.5$ limiting magnitude, contains 1,295,502 sources, while there is also a cleaner version with $G < 20.0$ limiting magnitude and 755,850 quasars. The spectro-photometric redshifts in the catalog are improved by training a k-nearest neighbors model on SDSS redshifts, achieving estimates on the $G < 20.0$ sample with only $\sim 10\%$ catastrophic redshift errors such that $|\Delta z/(1+z)| > 0.1$. In our case, we use the $G < 20.5$ sample, for which $\sim 70\%$ of the sources agree to $|\Delta z/(1+z)| < 0.1$ and $\sim 62\%$ to $|\Delta z/(1+z)| < 0.01$.

Together with the catalogs, a selection function map in HEALpix format is also provided, containing the probability that a source observed in that pixel would be included in the catalog, as well as a random catalog downsampled by the selection function containing about 10 times the number of Quaia QSO, and some observational systematics templates. For our analysis, we split the Quaia $G < 20.5$ sample in two redshift bins as in Fabbian et al. (2025). These two redshift bins are equally populated, splitting the sample around $z \sim 1.5$ and having average redshifts $\bar{z} = 0.97$, $\bar{z} = 2.10$. We impose the selection function to be larger than 0.5 to avoid low completeness regions close to the galactic plane, which could introduce systematics. To take into account the redshift uncertainties when splitting the sample in two redshift bins, we compute the redshift distributions as the sum at every redshift of Gaussian photo-z functions for each QSO given its observed redshift and redshift uncertainty. Accounting for the redshift uncertainties is also important in particular for the ARF theory estimations, since it decreases the measured signal. In this case we take into account the average redshift uncertainty of the Quaia $G < 20.5$ catalog, which is $\sigma_z \simeq 0.06(1+z)$, for the theoretical ARF model (see Sec. 4.2 for more details). We show in Fig. 1 the redshift distribution of the $G < 20.5$ two redshift bins together with the full sample distribution. The catalogs, the selection functions and all related materials are publicly available².

² <https://zenodo.org/records/10403370>

3.2. Planck CMB lensing

The second ingredient in our analysis is the *Planck* CMB lensing potential map. We use the *Planck* PR4 reconstruction of the CMB lensing potential (Carron et al. 2022), obtained from the *Planck* NPIPE temperature and polarization maps (Akrami et al. 2020). In particular, we use the minimum-variance estimate from temperature and polarization, after mean-field subtraction of the lensing convergence. This latest release of CMB lensing maps improves the noise with respect to the previous *Planck* PR3 maps (Planck Collaboration et al. 2020); and in particular, the large scale noise is lower and the mean-field is better understood thanks to the use of a larger number of simulations. The maps and the mask are publicly available³.

Note that the CMB lensing map does not include the Monte Carlo multiplicative correction applied in Carron et al. (2022). We compute this correction based on simulations as in Fabbian et al. (2025) using mode decoupled pseudo- C_ℓ , and apply the result as a multiplicative correction to the measured cross-correlations with the CMB lensing power spectra, C_ℓ^{kg} and C_ℓ^{kz} . This correction cannot be applied in a general way, since it depends on the footprint mask for each tracer involved in the analysis due to local variations of the normalization. The order of this correction is generally $\lesssim 5\%$, but it is larger ($\gtrsim 10\%$) for the lowest multipoles, having for this reason a non-negligible impact on the f_{NL} measurement.

4. Analysis pipeline

In this section we describe the pipeline implemented to measure the density and ARF observables from the Quaia catalog and jointly analyze them, together with the *Planck* CMB lensing data. The steps include creating maps and measuring the 2D angular power spectra, using a modification of the CAMB Boltzmann code (Lewis & Challinor 2011) to generate a theoretical model, generation of correlated mock fields to compute the covariance matrix, a validation of scale cuts through systematics deprojection and a Monte-Carlo Markov Chain likelihood code for parameter inference.

We start by creating HEALpix (Gorski et al. 2005) maps of the density and ARF fields using the $G < 20.5$ limiting magnitude Quaia QSO catalog. For the density maps, we compute the galaxy overdensity field in each pixel as $\delta_g = \rho/\bar{\rho} - 1$, where ρ is the QSO number counts after being corrected for the Quaia selection function. We impose a threshold of 0.5 in the selection function and mask out the sky regions with lower values to avoid low-completeness areas, which could potentially add systematics to the analysis. The final footprint after the selection function cut covers $\sim 60\%$ of the sky. For the ARF maps, the redshift fluctuation field in each pixel is defined as $\delta z = \sum_i (z_i - \bar{z})/\bar{\rho}$. We create both maps using a resolution $N_{\text{side}} = 128$. This choice is done in order to avoid having empty pixels without any QSO, which is needed to properly compute the ARF estimator. The procedure is implemented for each of the low-redshift and high-redshift bins shown in Fig. 1. We show the final masks and maps of the density and ARF fields for the low- z and high- z redshift bins Quaia sample in Fig. 2.

4.1. Angular power spectra

In order to estimate the angular power spectra of the Quaia density, ARF and their cross-correlation, as well as the cross-

³ https://github.com/carronj/planck_PR4_lensing/releases/tag/Data

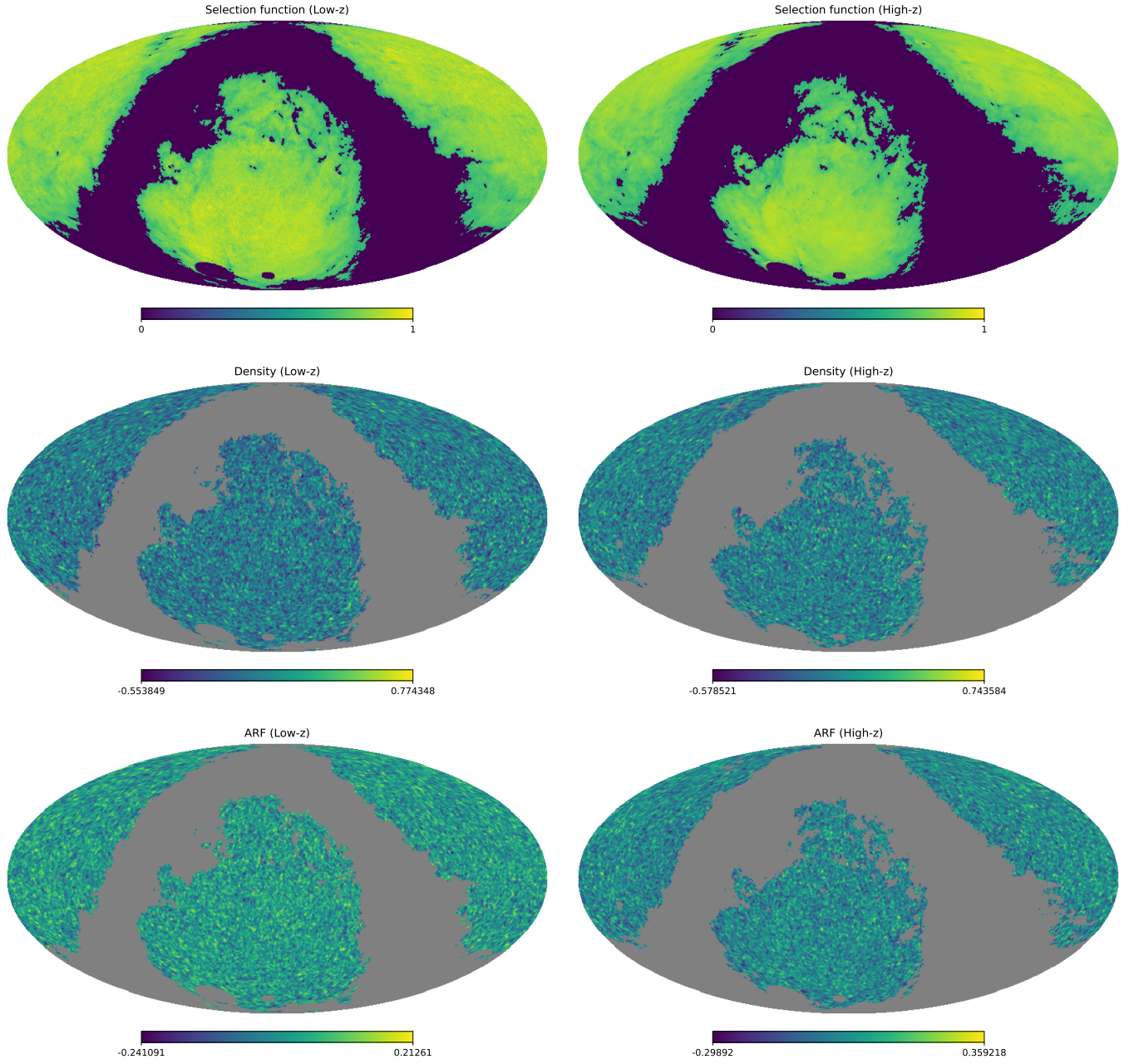


Fig. 2. Upper panels: normalized masks from the Quaia selection functions applied in our analysis after applying a 0.5 threshold for the low-z and high-z redshift bins. Middle panels: Quaia density maps for the low-z and high-z redshift bins. Lower panels: Quaia ARF maps for the low-z and high-z redshift bins. The density and ARF maps are represented with a 1 degree beam smoothing.

correlations with the *Planck* lensing, we use the pseudo- C_ℓ approach implemented in the publicly available NaMaster code (Alonso et al. 2019). The pseudo- C_ℓ of a pair of fields is defined as

$$\tilde{C}_\ell^{XY} = \frac{1}{2\ell + 1} \sum_m X_{\ell m} Y_{\ell m}^* \quad (16)$$

where $X, Y \equiv g, z, \kappa$ are the observed fields. Then, the difference between the true and measured C_ℓ due to the effects of the mask is taken into account through the mode-coupling matrix $M_{\ell\ell'}$ as

$$\langle \tilde{C}_\ell \rangle = \sum_{\ell'} M_{\ell\ell'} C_{\ell'} . \quad (17)$$

In practice, the inversion of the $M_{\ell\ell'}$ matrix is done using the MASTER algorithm (Hivon et al. 2002), which requires a discrete binning of the angular power spectrum. We use the implementation in the `compute_full_master` function in the NaMaster code to calculate the angular power spectra, and we bin the theory curves using the same bandpower window functions. For our analysis, we set a multipole binning of $\Delta\ell = 2$ for $\ell \leq 40$, $\Delta\ell = 5$ for $40 < \ell \leq 60$ and $\Delta\ell = 30$ for $\ell > 60$. This binning scheme is also used in Alonso et al. (2025); Fabbian et al. (2025) and intends to provide a good enough sampling of the angular power spectra at the lower multipoles where the f_{NL} signal arises. For the masks, we use the selection function with a 0.5 threshold for the Quaia observables and the *Planck* PR4 mask for the CMB lensing.

Note that the *Planck* PR4 CMB lensing maps are provided at resolution $N_{\text{side}} = 2048$, while we use Quaia maps at resolution $N_{\text{side}} = 128$. To overcome this issue, when computing the Quaia cross-correlations with the CMB lensing, C_{ℓ}^{kg} and C_{ℓ}^{kz} , we filter out the multipoles larger than $3N_{\text{side}} - 1$ from the *Planck* lensing $a_{\ell m}$ and generate a lensing map from this filtered $a_{\ell m}$ at resolution $N_{\text{side}} = 128$. We do not use any mask apodization for the Quaia observables, but instead apodize the *Planck* mask using the `mask_apodization` routine in `NaMaster`, with the ‘C1’ apodization type and a 0.2 degree scale.

Given the low QSO density of our sample, we compute and subtract the Poisson shot noise from the autocorrelation power spectra of the density and ARF, C_{ℓ}^{gg} and C_{ℓ}^{zz} . For this, we estimate the shot noise by computing the density and ARF angular power spectra from 25 random catalogs generated according to the Quaia selection functions. We show in Fig. 3 the auto-correlation power spectra C_{ℓ}^{gg} and C_{ℓ}^{zz} , and the CMB lensing cross-correlation power spectra in Fig. 4 (C_{ℓ}^{kg} and C_{ℓ}^{kz}). Note that in this paper we do not include as observable the cross-correlation between density and ARF, C_{ℓ}^{gz} , since it is a very weak signal that we found to be deviated with respect to the theoretical model even at high multipoles, which is a hint of correlated systematics.

4.2. Theoretical model

Our theoretical model for the angular power spectra is based on a modification of the CAMB Boltzmann code (Lewis & Challinor 2011). This modification includes the computation of ARF as new observable, in addition to the already existing LSS observables in the code (galaxy number counts, weak lensing and 21 cm intensity). It also includes the possibility of introducing the width of the photometric redshift (photo- z) probability density distribution (PDF) under the Gaussian and Lorentzian approximations, since photo- z errors considerably affect the amplitude of the ARF angular power spectra (Hernández-Monteagudo et al. 2024). For the case of the Quaia $G < 20.5$ sample analyzed in this work, we take into account the average redshift uncertainty of the catalog, $\sigma_z \simeq 0.06(1+z)$, in the ARF theory computations. The code is called `ARFCAMB` and includes as well the implementation of f_{NL} as an input parameter that enters in the scale-dependent bias. More details about the `ARFCAMB` code can be found in Lima-Hernández et al. (2022).

We generated the theoretical angular power spectra of our observables and their cross-correlations using the `ARFCAMB` code assuming a fiducial $f_{\text{NL}} = 0$, and the rest of the cosmological parameters were fixed to the *Planck* 2018 cosmology *Planck Collaboration et al.* (2020), i.e. $\Omega_b h^2 = 0.022383$, $\Omega_c h^2 = 0.12011$, $H_0 = 67.32 \text{ km s}^{-1} \text{ Mpc}^{-1}$ and $\sigma_8 = 0.812$. For the window function of each redshift bin we used the dN/dz represented in Fig. 1 and a fiducial evolution of the galaxy bias as measured in Piccirilli et al. (2024), hereafter P24, for the Quaia sample. This evolution is parametrized through the expression

$$b_{\text{QSO}}(z) = b_0 / D(z), \quad (18)$$

with $b_0 = 1.26$ as fiducial value. As a consistency check, we also will consider the fiducial redshift evolution of the galaxy bias based in the eBOSS QSO model by Laurent et al. (2017), hereafter L17:

$$b_{\text{QSO}}(z) = 0.278 \left((1+z)^2 - 6.565 \right) + 2.393. \quad (19)$$

Observable		C_{ℓ}^{gg}		C_{ℓ}^{zz}	
Bin		Low- z	High- z	Low- z	High- z
P24 $b(z)$	ℓ_0	17	16	5	20
	β	1.73	1.19	2.99	3.59
L17 $b(z)$	ℓ_0	32	27	10	20
	β	1.50	1.87	1.87	3.57

Table 1. Derived ℓ_0 and β parameters of the model that we adopt for the excess of observed power in the C_{ℓ}^{gg} and C_{ℓ}^{zz} data, for the P24 and L17 fiducial bias evolution models.

4.3. Mocks and covariance matrix

We generate 1,000 correlated simulations for the density, ARF and CMB lensing fields in order to compute the covariance matrices and test the analysis pipeline. Our mock fields are created using the theoretical angular power spectra as input for the `healpy.synalm` function. The procedure for simulating N correlated fields is described in Giannantonio et al. (2008) and internally implemented in the `healpy.synalm` function. The $a_{\ell m}$ are then converted to maps with the `healpy.alm2map` function.

In our case, we will have $N = 5$ fields: density and ARF for the two Quaia redshift bins and CMB lensing, that are generated from $N(N + 1)/2 = 15$ input auto and cross-correlations between the 5 fields. To generate realistic covariance matrices, we implemented a correction in the autocorrelation power spectra C_{ℓ}^{gg} and C_{ℓ}^{zz} to account for the excess of measured power at the lower multipoles in the real data compared to the theory model due to potential systematics. This correction is applied only to generate mocks that reproduce the real data measurements and finally obtain the covariance matrix. The implementation is done with the following power law parameterization of the measured power spectra:

$$C_{\ell}^{\text{XX,measured}} \simeq C_{\ell}^{\text{XX,theory}} \left[1 + \left(\frac{\ell_0}{\ell} \right)^{\beta} \right] \quad (20)$$

where ℓ_0 and β are free parameters determined from the data. By fitting with a least squares method the data to Eq. 20, we obtain the ℓ_0 and β parameters listed in Tab 1, for each one of the redshift bins and fiducial bias models. We represent in Fig. 3 the comparison between the data and the theoretical model after applying this correction.

After generating the mock signal for the $N = 5$ correlated fields, we simulate the noise component. We include in the CMB lensing field another Gaussian map component based on the *Planck* PR4 lensing theoretical noise. We checked that this approach is compatible at $\lesssim 10\%$ level with the real measured C_{ℓ}^{kk} from the *Planck* PR4 data. For the density field, we convert the overdensity to predicted number counts per pixel using the Quaia data average density \bar{N} , and generate a discrete number of QSO in each pixel by Poisson sampling. For the computation of the ARF maps, we assign a redshift to each QSO by random sampling a Gaussian distribution centered in $\bar{z} + \delta z$ with a dispersion equal to the RMS of the redshift bins in the Quaia catalog, where δz is the predicted ARF field in the pixel.

We finally obtain the joint covariance matrix for our analysis by computing the power spectra of the 1,000 correlated simulations. We also cross-checked that the shot noise estimations with randoms for C_{ℓ}^{gg} and C_{ℓ}^{zz} are accurate, by recovering the input theoretical power spectra after subtracting the noise from the measured C_{ℓ}^{gg} and C_{ℓ}^{zz} from the mocks.

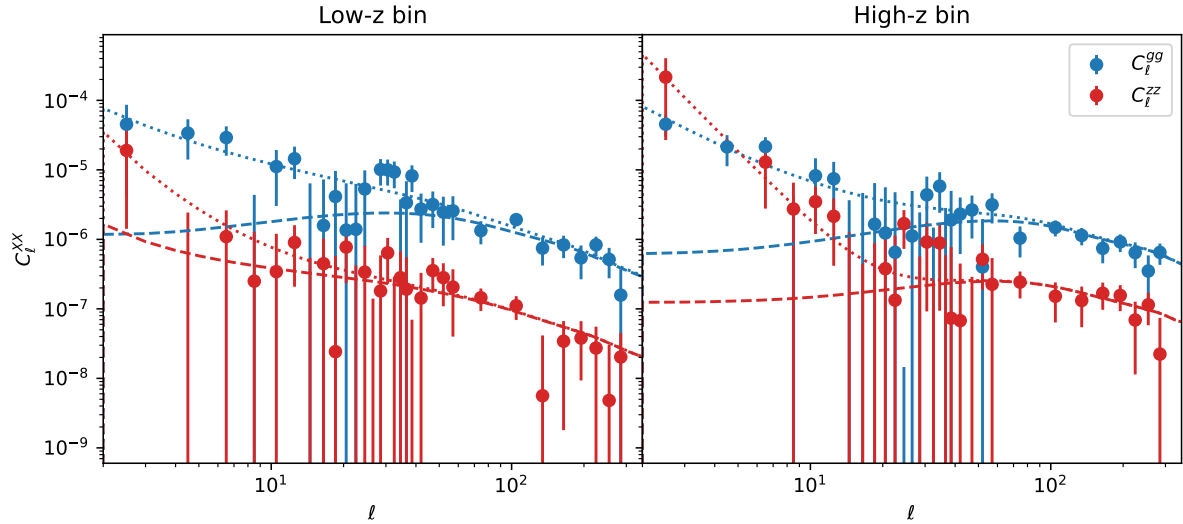


Fig. 3. Measured angular power spectra of the Quaia density and ARF autocorrelations for the low redshift (left panel) and high redshift (right panel) bins. The dots represent the binned angular power spectra with errorbars, the dashed lines the theoretical model with $f_{\text{NL}} = 0$, and the dotted lines the same model after the parametrization of the measured excess of power.

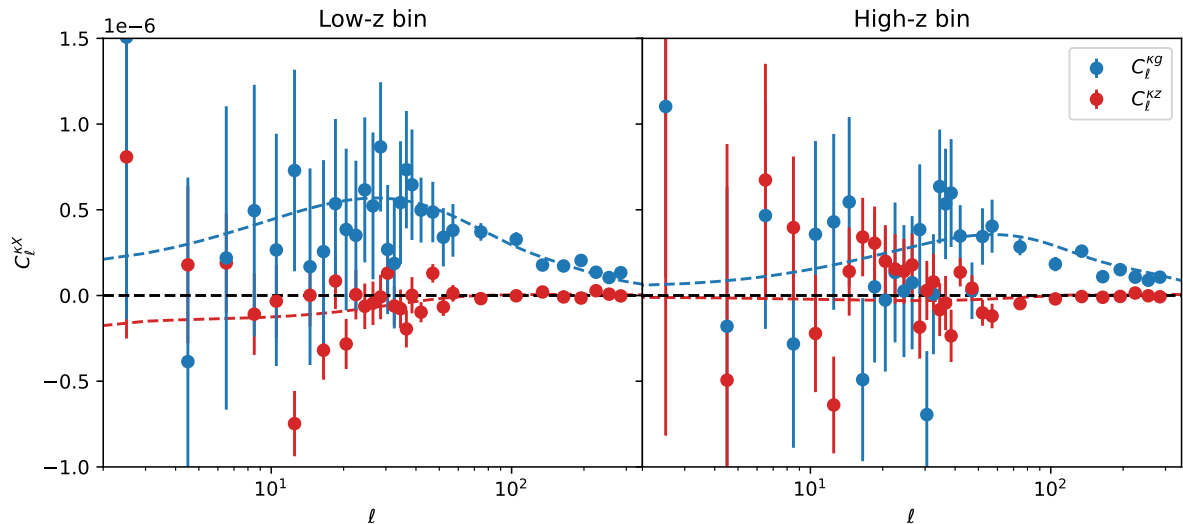


Fig. 4. Measured angular power spectra of the Quaia density and ARF cross-correlations with the *Planck* CMB lensing for the low redshift (left panel) and high redshift (right panel) bins. The dots represent the binned angular power spectra with errorbars and the dashed lines the theoretical fiducial model with $f_{\text{NL}} = 0$.

4.4. Systematics deprojection and scale cuts

We perform systematics deprojection tests on the data and on the mocks to validate the lower minimum multipoles that can be safely included in our analysis for each observable. For this, we use a joint linear regression for the full set of Quaia systematics templates based on the ordinary least squared (OLS) method introduced in, e.g., [Weaverdyck & Huterer \(2021\)](#). We apply the linear deprojection to our data, and to our 1000 mocks that do not contain any systematics. Thus, the variations on the angular power spectra after deprojecting systematics from the mocks are explained as random fluctuations. In this way, we compare the ΔC_ℓ difference at each scale for the data to the ΔC_ℓ distribution for the mocks, and determine that a given multipole is affected by systematics if its variation cannot be explained as statistical fluctuation at 95% confidence level.

In [Fabbian et al. \(2025\)](#), it is already discussed that the measured C_ℓ^{kg} from Quaia and *Planck* data present compatible deviations from the model with random fluctuations at every multipole, while C_ℓ^{gg} present offsets at large scales ($\ell \lesssim 15$) that cannot be explained as statistical fluctuation. Here, for the density and its CMB lensing cross-correlation we adopt the same validated scale cuts in [Fabbian et al. \(2025\)](#) and set $\ell_{\text{min}} = 14$ for C_ℓ^{gg} and $\ell_{\text{min}} = 2$ for C_ℓ^{kg} . For the ARF, we validate the cuts with our regression method and find that for C_ℓ^{kz} the offset in the data is compatible with statistical fluctuations at every multipole, while for C_ℓ^{zz} , scales lower than $\ell \lesssim 10$ present larger offsets than those compatible with the mocks at 95% confidence level. In Fig. 5 we represent an example of this validation of the shift in C_ℓ^{zz} and C_ℓ^{kz} for $\ell = 6$ and $\ell = 10$, using the Quaia high-z sample.

ARF could have a different sensitivity to systematics, since they rely not only on the number of QSOs detected in a given

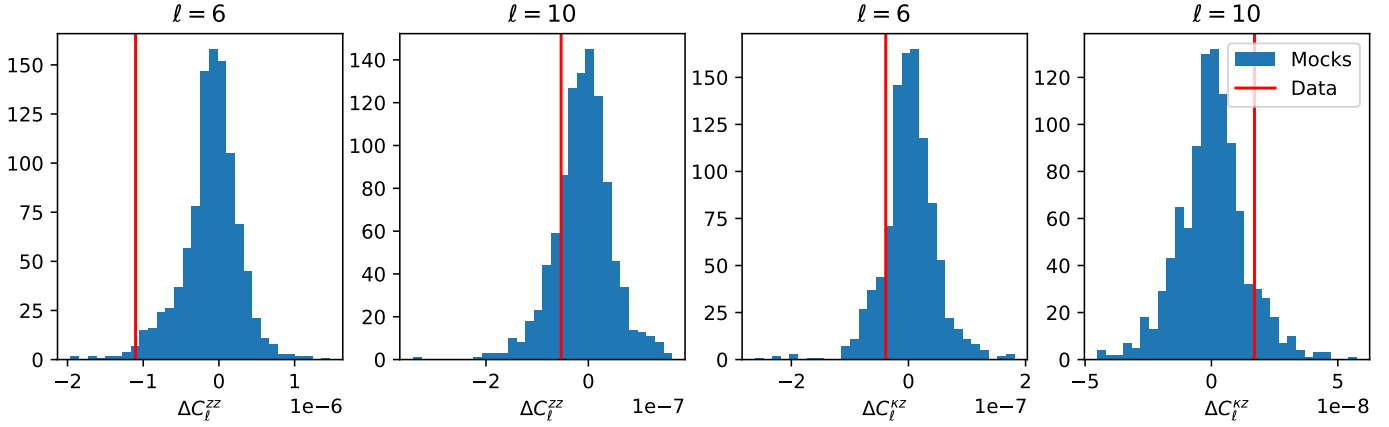


Fig. 5. Comparison of the shift on the $\ell = 6$ and $\ell = 10$ angular power spectra of the Quaia high-z sample after applying systematics deprojection to the mocks and data for C_ℓ^{zz} (left panels) and $C_\ell^{\kappa z}$ (right panels), used to validate the scale cuts in our analysis. The blue bars represent the distribution of the shift on the 1000 mock realizations and the red lines the shift found in real data.

pixel, but also on their measured photo-zs. The quality of the photo-z estimates typically depends upon photometric conditions that also modulate the number of detected sources, such as airmass, sky background, and extinction. Nevertheless, there may exist other aspects that could modulate the photo-z quality, and in the particular case of QSOs, the real QSO redshift is one of them: line confusion –which is the main cause for QSO catastrophic photo-z assignments– is more likely for QSOs below $z \approx 2.1$ than for QSOs with above this redshift, since for the latter the (bright) Lyman- α enters Gaia's optical system. Such modulation should be present mainly in the lower redshift bin under consideration, which has a lower weight given in our analysis the bias redshift dependence.

Note that our baseline angular power spectra for the analysis are those before systematics deprojection. Since for multipoles larger than our scale cuts the measured angular power spectra after deprojection is compatible with random fluctuations, we consider enough to remove the lower multipoles as strategy to overcome observational systematics.

4.5. Likelihood and parameter inference

We define the likelihood \mathcal{L} as a multivariate Gaussian

$$-2 \log \mathcal{L} \equiv \chi^2 = \sum_{\ell, \ell'} \left(C_\ell^{\text{obs}} - \tilde{C}_\ell(\theta) \right) \text{Cov}_{\ell \ell'}^{-1} \left(C_{\ell'}^{\text{obs}} - \tilde{C}_{\ell'}(\theta) \right) \quad (21)$$

where C_ℓ^{obs} are the elements of the data vector, $\tilde{C}_\ell(\theta)$ is the theoretical model of the angular power spectrum for a given set of parameters θ and Cov^{-1} is the inverse of the covariance matrix. We consider safe enough the Gaussian likelihood approximation, since in [Alonso et al. \(2023\)](#) it is demonstrated that the distribution of the QSO - CMB lensing cross-correlation measurements (and the auto-correlation for small scales) are well described by a Gaussian. Our theoretical model is based in the ARFCAMB code described in Sect. 4.2. In order to account for possible uncertainties on the galaxy bias modeling, we adopt an extension of the parametrization of the Quaia $b(z)$ by [Piccirilli et al. \(2024\)](#) expressed in Eq. 18:

$$b(z) = \frac{b_0}{D(z)} (1+z)^\alpha \quad (22)$$

where b_0 and α are free parameters, and the $b_0 = 1.26, \alpha = 0$ case reduces to the fiducial bias evolution model by [Piccirilli](#)

[et al. \(2024\)](#). To compute the constraints on the cosmological parameters, we implement our likelihood using the Monte Carlo Markov Chain (MCMC) sampler `emcee`⁴ ([Foreman-Mackey et al. 2013](#)). Our analysis includes f_{NL} and the bias parameters b_0 and α as the three cosmological parameters to constrain. The rest of the cosmological parameters are fixed to the *Planck* 2018 cosmology [Planck Collaboration et al. \(2020\)](#).

We use as minimum multipoles $\ell_{\text{min}} = 2$ for $C_\ell^{\kappa g}$ and $C_\ell^{\kappa z}$, $\ell_{\text{min}} = 14$ for C_ℓ^{gg} and $\ell_{\text{min}} = 10$ for C_ℓ^{zz} , according to the tests discussed in Sec. 4.4. For the maximum multipoles we set $\ell_{\text{max}} = 300$ for the High-z redshift bin, and we cut the Low-z bin in $\ell_{\text{max}} = 240$ to avoid including k -modes larger than $k \sim 0.07 h \text{ Mpc}^{-1}$. Although for the High-z bin the $k \sim 0.07 h \text{ Mpc}^{-1}$ cutoff would correspond to $\ell \lesssim 400$, we decided not to include any multipole larger than 300 in the analysis given the limited resolution of our maps ($N_{\text{side}} = 128$). In our theoretical model, from ARFCAMB we also included non-linear contributions to the power spectrum using `halofit` ([Takahashi et al. 2012](#)). Furthermore, for a proper comparison with the theory model, we correct our data for the pixel window function, given that its impact is not negligible for $\ell_{\text{max}} \gtrsim 2N_{\text{side}}$.

5. Results

We calculated the constraints on f_{NL} and the b_0, α bias model parameters individually for the four observables involved in our analysis ($C_\ell^{gg}, C_\ell^{\kappa g}, C_\ell^{zz}$ and $C_\ell^{\kappa z}$). The median likelihood values with 68% confidence intervals are reported in Tab. 2, together with the two combinations of density and ARF with their respective CMB lensing cross-correlations and the joint analysis of the four observables. The measured constraints before adding ARF, just considering $C_\ell^{gg} + C_\ell^{\kappa g}$, are consistent with the findings by [Fabbian et al. \(2025\)](#), where they report $f_{\text{NL}} = -20.5^{+19.0}_{-18.1}$ assuming the universality relation with $p = 1$. As in [Fabbian et al. \(2025\)](#), our joint constraint from density and CMB lensing is dominated by $C_\ell^{\kappa g}$ due to the Poisson shot noise limitations of the Quaia sample for C_ℓ^{gg} . Instead, for the $C_\ell^{zz} + C_\ell^{\kappa z}$ constraints, we find that the ARF autocorrelation C_ℓ^{zz} is the dominant term in the joint analysis. This makes sense provided that, for ARF, the cross-angular power spectrum multipoles $C_\ell^{\kappa z}$ are very close to zero for all but for low ℓ s, which are dominated by cosmic

⁴ <https://emcee.readthedocs.io/>

Observ.	f_{NL}	b_0	α	χ^2/dof
C_{ℓ}^{gg}	-51^{+37}_{-39}	0.93 ± 0.14	$0.33^{+0.18}_{-0.16}$	42/45
C_{ℓ}^{zz}	-93^{+43}_{-26}	$0.53^{+0.13}_{-0.12}$	$0.83^{+0.25}_{-0.26}$	39/49
C_{ℓ}^{kg}	-16^{+22}_{-23}	$0.96^{+0.15}_{-0.13}$	0.23 ± 0.17	63/57
C_{ℓ}^{kz}	187^{+516}_{-144}	$1.49^{+0.77}_{-0.54}$	$0.02^{+0.29}_{-0.45}$	105/57
$C_{\ell}^{gg} + C_{\ell}^{kg}$	-25^{+19}_{-17}	$1.01^{+0.10}_{-0.09}$	$0.20^{+0.11}_{-0.10}$	113/105
$C_{\ell}^{zz} + C_{\ell}^{kz}$	-43^{+50}_{-44}	$0.67^{+0.09}_{-0.10}$	$0.55^{+0.19}_{-0.17}$	164/109
$C_{\ell}^{gg} + C_{\ell}^{kg}$ + $C_{\ell}^{zz} + C_{\ell}^{kz}$	-3 ± 14	0.83 ± 0.06	0.37 ± 0.09	338/217

Table 2. Median likelihood cosmological parameters with 1σ confidence intervals for the baseline analysis from the four observables involved in our analysis and their combinations. We also list the χ^2 per degrees of freedom for each case.

variance. We measure $f_{\text{NL}} = -43^{+50}_{-44}$ from ARF and its cross-correlation with CMB lensing, and when we combine this information with the Quaia density and its cross-correlation with CMB lensing, we find $f_{\text{NL}} = -3 \pm 14$. The result represents a $\sim 25\%$ improvement with respect to the measurement in Fabbian et al. (2025) from $C_{\ell}^{gg} + C_{\ell}^{kg}$, consistently with the expected theoretical impact of ARF in the constraints (see Appendix B for more details). Our measurement is the second most precise constraint on f_{NL} from LSS using two-point functions to date, after the Chaussidon et al. (2025) measurement using DESI DR1 spectroscopic data ($\sigma(f_{\text{NL}}) \sim 9$). We represent in Fig. 6 the comparison of the constraints on the parameters from $C_{\ell}^{gg} + C_{\ell}^{kg}$, $C_{\ell}^{zz} + C_{\ell}^{kz}$ and their combination.

In Tab. 2 we appreciate some mild tensions between the best-fit model and the observed data, reported by the χ^2 per degrees of freedom (dof) estimates in the right column. In the case of C_{ℓ}^{kz} , it is mainly due to a few data points, as for example at $\ell \simeq 12$ data point, which lies more than 3σ off the preferred models (see Fig. 4). We checked that if we remove these data points from the analysis, the reduced χ^2 values of the combined analysis become much better (see more details in Appendix A). There exists also some moderate tension ($\lesssim 2\sigma$) between the bias parameter estimates from C_{ℓ}^{zz} and C_{ℓ}^{kz} . The tension also appears when we compare the combinations $C_{\ell}^{gg} + C_{\ell}^{kg}$ and $C_{\ell}^{zz} + C_{\ell}^{kz}$. We believe this is caused by the higher sensitivity of the ARF kernel to higher k -modes (or non-linear scales), something that impacts more C_{ℓ}^{zz} than C_{ℓ}^{kz} . This point will be elaborated on further below.

To investigate whether these tensions could be related to degeneracies between parameters and to test the stability of the b_0 and α measurements, we recompute the constraints on the three parameters from $C_{\ell}^{gg} + C_{\ell}^{kg}$ and $C_{\ell}^{zz} + C_{\ell}^{kz}$ using $\ell_{\text{min}} = 20$ and $\ell_{\text{min}} = 40$. The purpose of these scale cuts is to remove the larger scales where the f_{NL} sensitivity arises, leaving only small-scale information which is sensitive to the galaxy bias. We list the constraints with these ℓ_{min} cuts and compare them to the baseline case with lower ℓ_{min} in Tab. 3. We find the constraints from $C_{\ell}^{zz} + C_{\ell}^{kz}$ are stable to the scale cuts. For $C_{\ell}^{gg} + C_{\ell}^{kg}$, we find hints of a trend in which we measure larger α parameters with the higher ℓ_{min} cuts. Although it is not statistically significant, this trend is consistent with what is expected when more weight is given to smaller, potentially non-linear scales.

To understand whether the tension on the bias parameters could be related to limits on the modeling of non-linear scales, we also compute the constraints from $C_{\ell}^{gg} + C_{\ell}^{kg}$ and $C_{\ell}^{zz} + C_{\ell}^{kz}$ with an $\ell_{\text{max}} = 200$ cut. We compare in Tab. 4 the results to the baseline case. We find that the measurement from $C_{\ell}^{gg} + C_{\ell}^{kg}$ is stable

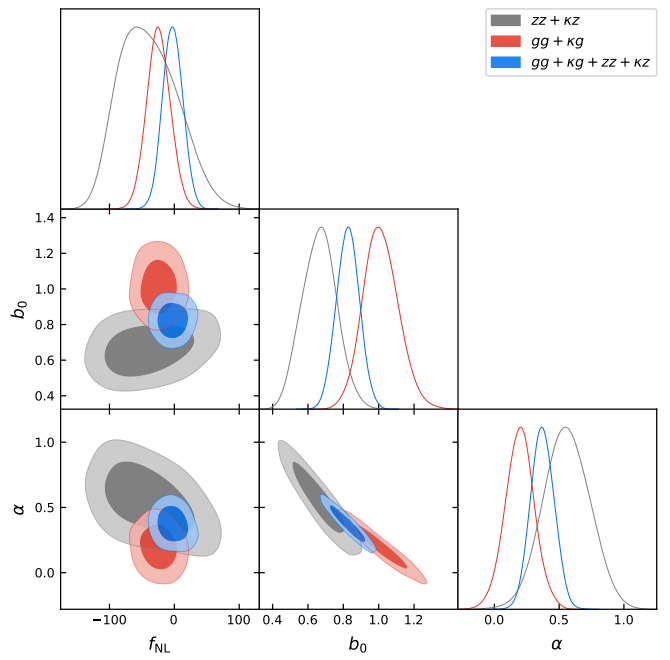


Fig. 6. 1σ and 2σ confidence ellipses for f_{NL} and the b_0 and α bias parameters measured from Quaia and *Planck* data, assuming the same bias parameterization for density and ARF (baseline case). The grey contours represent the constraints from ARF plus their CMB lensing cross-correlation, the red contours represent the density plus their CMB lensing cross-correlation, and the blue contours represent the combination of density, ARF and their CMB lensing cross-correlations.

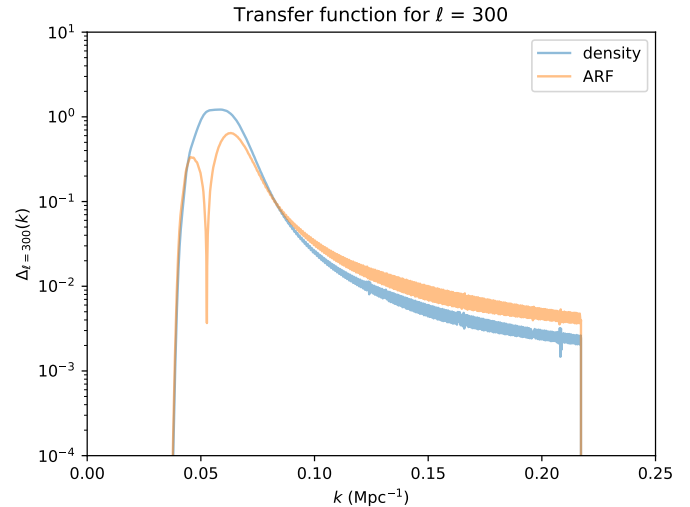


Fig. 7. Transfer function for the density (blue line) and ARF (orange line) fields obtained assuming the high-z Quaia sample for $\ell = 300$, as a function of the k scale.

with ℓ_{max} ; instead, the bias parameters measured from $C_{\ell}^{zz} + C_{\ell}^{kz}$ vary when adopting a lower ℓ_{max} and the tension between observables is alleviated. This suggests that the discrepancy on the bias measurement is related to the higher impact of smaller (and potentially non-linear) scales on the ARF kernel under the same redshift window function. This is somewhat expected, since the ARF kernel can be seen as a radial gradient of the 3D density field *under* the redshift shell, and, unlike the density kernel, is sensitive to variations of the quasar density field under the redshift window (see Hernández-Monteagudo et al. 2020a, for fur-

Observables	ℓ_{\min}	f_{NL}	b_0	α
$C_{\ell}^{gg} + C_{\ell}^{kg}$	14, 2	-25^{+19}_{-17}	$1.01^{+0.10}_{-0.09}$	$0.20^{+0.11}_{-0.10}$
	20	-93^{+29}_{-25}	0.83 ± 0.07	0.45 ± 0.11
	40	-43^{+44}_{-45}	0.77 ± 0.07	$0.52^{+0.10}_{-0.12}$
$C_{\ell}^{zz} + C_{\ell}^{kz}$	10, 2	-43^{+50}_{-44}	$0.67^{+0.09}_{-0.10}$	$0.55^{+0.19}_{-0.17}$
	20	-16^{+59}_{-56}	$0.75^{+0.08}_{-0.07}$	$0.42^{+0.14}_{-0.17}$
	40	-36^{+86}_{-76}	$0.79^{+0.12}_{-0.13}$	$0.37^{+0.20}_{-0.19}$

Table 3. Median likelihood cosmological parameters with 1σ confidence intervals for the $C_{\ell}^{gg} + C_{\ell}^{kg}$ and $C_{\ell}^{zz} + C_{\ell}^{kz}$ observables as a function of the minimum multipole(s) used in the analysis.

Observables	ℓ_{\max}	f_{NL}	b_0	α
$C_{\ell}^{gg} + C_{\ell}^{kg}$	240, 300	-25^{+19}_{-17}	$1.01^{+0.10}_{-0.09}$	$0.20^{+0.11}_{-0.10}$
	200	-9^{+29}_{-26}	$1.03^{+0.13}_{-0.12}$	0.12 ± 0.15
$C_{\ell}^{zz} + C_{\ell}^{kz}$	240, 300	-49^{+53}_{-36}	$0.63^{+0.10}_{-0.08}$	0.60 ± 0.17
	200	95^{+117}_{-89}	$0.95^{+0.16}_{-0.13}$	$0.02^{+0.22}_{-0.25}$

Table 4. Median likelihood cosmological parameters with 1σ confidence intervals for the $C_{\ell}^{gg} + C_{\ell}^{kg}$ and $C_{\ell}^{zz} + C_{\ell}^{kz}$ observables as a function of the maximum multipole used in the analysis.

ther details). To illustrate this, in Fig. 7 we represent the transfer function for $\ell = 300$ assuming the high- z Quaia sample, where it is shown that for ARF the sensitivity of the transfer function for higher k -modes is larger compared to the density: not only due to its higher amplitude at high k values, but also due to the sign flip at $k \sim 0.07 \text{ Mpc}^{-1}$. This suggests future work will be needed to improve the modeling of non-linear scales in ARF; however, our scope in this work is to effectively quantify the impact on the f_{NL} determination of these sources of systematics.

To quantify the effect on the constraints on f_{NL} of the assumptions related to the fiducial galaxy bias evolution, we recomputed the joint constraints on f_{NL} including all observables changing the baseline assumptions. The tests included the assumption of an underlying bias redshift evolution following $\alpha = 0$ as measured in P24, and the use of a different bias evolution such as the eBOSS model by L17. Furthermore, to test whether the tensions on b_0 and α between observables caused by non-linear scales modeling have an impact on the final results, we also consider a case in which we vary two pairs of the b_0 and α parameters, one for C_{ℓ}^{gg} and C_{ℓ}^{kg} and another for C_{ℓ}^{zz} and C_{ℓ}^{kz} , such that the non-linear physics are parametrized in an effective bias for each field. The results of these tests are listed in Tab. 5. For the P24 and L17 bias models, instead of varying the b_0 and α parameters, we fit two amplitude parameters A_1 and A_2 for each redshift bin. For all the tests, we obtained compatible results with almost no shift in the measured f_{NL} and similar confidence intervals. We concluded from these checks that our result is robust against the fiducial assumptions on the $b(z)$ evolution model. In particular, for the test with two pairs of bias parameters, we find $f_{\text{NL}} = -6^{+15}_{-14}$, a similar errorbar to the baseline case ($f_{\text{NL}} = -3 \pm 14$), and the values of each b_0 and α are compatible with those of the baseline cases for $C_{\ell}^{gg} + C_{\ell}^{kg}$ and $C_{\ell}^{zz} + C_{\ell}^{kz}$ reported in Tab. 2. This shows that our constraints on f_{NL} are stable when the shift on the b_0 and α parameters is reduced or eliminated, and therefore our results are not artificially enhanced by the tension between observables on the bias parameters. We show the constraints on the parameters assuming two separate bias parameterizations in Fig. 8.

	f_{NL}	b_0	α
Baseline	-3 ± 14	0.83 ± 0.06	0.37 ± 0.08
	f_{NL}	$b_0^g (b_0^z)$	$\alpha^g (\alpha^z)$
Separate b_0 and α	-6^{+15}_{-14}	0.92 ± 0.09 (0.73 ± 0.10)	0.27 ± 0.12 (0.41 ± 0.14)
	f_{NL}	A_1	A_2
P24 $b(z)$	-2^{+14}_{-16}	1.05 ± 0.03	1.24 ± 0.04
L17 $b(z)$	-4 ± 14	1.05 ± 0.03	$0.97^{+0.03}_{-0.04}$

Table 5. Median likelihood cosmological parameters with 1σ confidence intervals for the baseline analysis of the combination of observables compared to different assumptions on the $b(z)$ fiducial evolution and number of parameters.

We have assumed the universality relation with $p = 1$ as baseline for computing the theoretical f_{NL} impact on the scale dependent bias. However, several works in the literature (e.g. Slosar et al. 2008) state that $p = 1.6$ is a more realistic value for the response of the QSO bias to f_{NL} . Furthermore, recent works such as Barreira (2020, 2022) state that given the uncertainties in the p parameter we can only determine $b_{\phi} f_{\text{NL}}$ through LSS measurements. To bracket the impact on the f_{NL} constraints of the possibility of having a lower response of QSO to the local PNG parameter, we recomputed the constraints from the joint analysis of all observables assuming $p = 1.6$, and we also measured the independent $b_{\phi} f_{\text{NL}}$ constraints from the same data. We obtained $f_{\text{NL}} = 2^{+20}_{-21}$ for the $p = 1.6$ case and $b_{\phi} f_{\text{NL}} = -63^{+79}_{-89}$ for the model-independent assumption.

In summary, we have shown that the improvement in the f_{NL} uncertainty due to the addition of ARF as a new observable is robust enough to the possible systematics in our analysis. The internal tensions between the observables suggest that ARF are more sensitive to non-linear physics under the same ℓ_{\max} scale cuts than 2D clustering, and future work will be needed to better model the non-linearities for ARF. However, in this work, we have shown that when parameterizing these uncertainties with an independent effective bias, our f_{NL} measurement remains unaffected. Our results are promising as the first application of this new cosmological observable to the measurement of f_{NL} from real data, and motivate that ARF should be included in the future analysis pipelines of 2D clustering, in particular for surveys that will be analyzed in the 2D harmonic space like LSST or the Euclid photometric survey. On the other hand, a 2D analysis of spectroscopic surveys like DESI could be improved with the inclusion of ARF, which should be a more robust observable with zero or negligible photometric redshift uncertainties, and this will provide a 2D alternative to the standard 3D clustering analysis with additional constraining power.

6. Conclusions

In this work we have studied, for the first time on real data, the sensitivity of ARF, a new 2D observable that measures matter tracers' redshift angular deviations as a cosmological probe, to the local primordial non-Gaussianity parameter f_{NL} . Using the Quaia QSO catalog, constructed from Gaia and unWISE data, we have extended a previous analysis in which f_{NL} was measured from the Quaia QSO density and its cross-correlation with the *Planck* PR4 CMB lensing to include ARF as an additional cosmological probe.

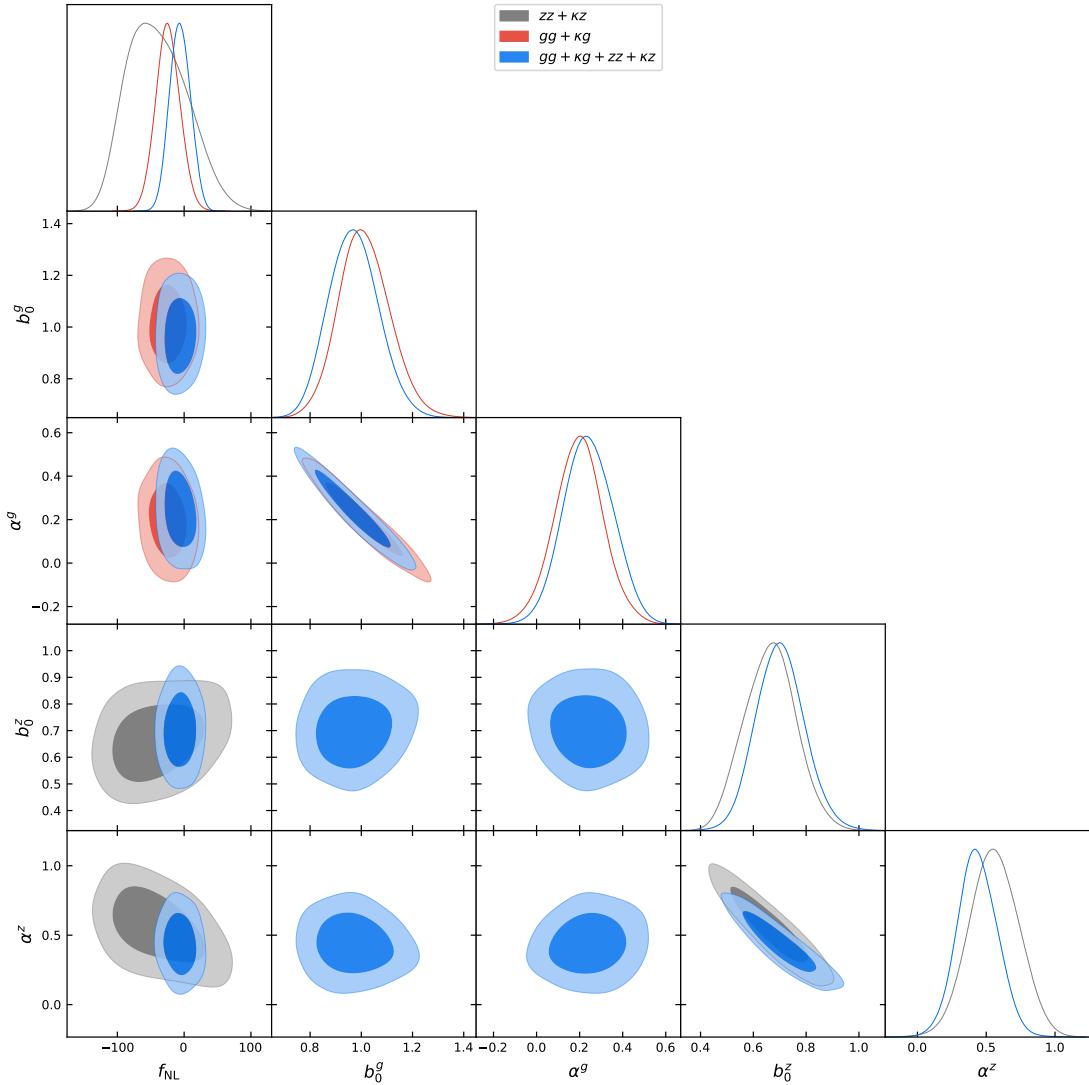


Fig. 8. 1σ and 2σ confidence ellipses for f_{NL} and the b_0 and α bias parameters measured from Quaia and *Planck* data, assuming two independent bias parameterizations for density and ARF. The grey contours represent the constraints from ARF plus their CMB lensing cross-correlation, the red contours represent the density plus their CMB lensing cross-correlation, and the blue contours the combination of density, ARF and their CMB lensing cross-correlations.

We have developed an analysis pipeline based on a modification of the CAMB Boltzmann code, and we have used that theoretical model to generate correlated simulations of the three fields involved in our analysis: CMB lensing, density and ARF. To deal with the possible presence of systematics in the auto power spectra of density and ARF we have implemented scale cuts in the analysis and fitted a power law model to the measured auto power spectra to generate a realistic covariance matrix.

Assuming the universality relation with $p = 1$, just from the Quaia ARF and their cross-correlation with the *Planck* CMB lensing, we have obtained $f_{\text{NL}} = -43^{+50}_{-44}$. We have also measured $f_{\text{NL}} = -25^{+19}_{-17}$ from the Quaia density and its cross-correlation with *Planck* lensing, a constraint that is fully consistent with the results in Fabbian et al. (2025). By combining Quaia density, ARF and their respective CMB lensing cross-correlations, we obtain as joint constraint $f_{\text{NL}} = -3 \pm 14$, which represents a $\sim 25\%$ improvement thanks to the addition of ARF. Despite the internal tensions on the measured galaxy bias parameters from different observables, we have checked that our constraint is robust enough against the different assumptions for the evolution

of the galaxy bias, including fitting an independent effective bias model for ARF. Our result is the second tightest constraint on f_{NL} using LSS two-point functions to date, and the most precise obtained from projected 2D summary statistics.

Our study motivates the inclusion of ARF as an extra cosmological probe in 2D analysis in the harmonic space with data from ongoing and future large-scale surveys such as DESI, Euclid and LSST. Among the future work that will be needed to improve future analyses including ARF, we remark it will be needed to have a better understanding of ARF systematics, which could be particularly important when using photometric redshifts, and this should allow to include observables like the cross-correlation between density and ARF. Furthermore, a better modeling of non-linearities in the ARF will be a key factor to perform a joint analysis with 2D galaxy density, given the higher sensibility of the ARF kernel to non-linear physics under the same multipoles.

Acknowledgements. JRBC, CHM, ACP, and JMC acknowledge the support of the Spanish Ministry of Science and Innovation under the grants PID2021-126616NB-I00 and “DarkMaps” PID2022-142142NB-I00, and from the Euro-

pean Union through the grant “UNDARK” of the Widening participation and spreading excellence program (project number 101159929). JRBC acknowledges support from a Momentum MSCA Fellowship, co-funded by the European Comission through the HORIZON-MSCA-2023-COFUND programme and the Secretariat of the Hungarian Academy of Sciences (MTA). We thank the members of the Quaia team and F. Bouchet for helpful feedback and discussions.

References

Adame, A. G., Avila, S., Gonzalez-Perez, V., et al. 2024, *Astron. Astrophys.*, 689, A69

Afshordi, N. & Tolley, A. J. 2008, *Physical Review D*, 78

Akrami, Y., Andersen, K. J., Ashdown, M., et al. 2020, *Astron. Astrophys.*, A42

Alonso, D., Bull, P., Ferreira, P. G., Maartens, R., & Santos, M. G. 2015, *The Astrophysical Journal*, 814, 145

Alonso, D., Fabbian, G., Storey-Fisher, K., et al. 2023, *Journal of Cosmology and Astroparticle Physics*, 2023, 043

Alonso, D., Hetmantsev, O., Fabbian, G., Slosar, A., & Storey-Fisher, K. 2025, *The Open Journal of Astrophysics*, 8

Alonso, D., Sanchez, J., & Slosar, A. 2019, *Mon. Not. Roy. Astron. Soc.*, 484, 4127

Asorey, J., Crocce, M., Gaztañaga, E., & Lewis, A. 2012, *Monthly Notices of the Royal Astronomical Society*, 427, 1891–1902

Bardeen, J. M., Steinhardt, P. J., & Turner, M. S. 1983, *Phys. Rev. D*, 28, 679

Barreira, A. 2020, *Journal of Cosmology and Astroparticle Physics*, 2020, 031–031

Barreira, A. 2022, *Journal of Cosmology and Astroparticle Physics*, 2022, 013

Bermejo-Clement, J. R., Ballardini, M., Finelli, F., et al. 2021, *Physical Review D*, 103

Bermejo-Clement, J. R., Demina, R., Krolewski, A., et al. 2025, *Astron. Astrophys.*, 698, A177

Cabass, G., Ivanov, M. M., Philcox, O. H. E., Simonović, M., & Zaldarriaga, M. 2022, *Phys. Rev. D*, 106, 043506

Cagliari, M. S., Castorina, E., Bonici, M., & Bianchi, D. 2024, *Journal of Cosmology and Astroparticle Physics*, 2024, 036

Camera, S., Fonseca, J., Maartens, R., & Santos, M. G. 2018, *Monthly Notices of the Royal Astronomical Society*, 481, 1251–1261

Carbone, C., Verde, L., & Matarrese, S. 2008, *The Astrophysical Journal*, 684, L1–L4

Carron, J., Mirmelstein, M., & Lewis, A. 2022, *Journal of Cosmology and Astroparticle Physics*, 2022, 039

Castorina, E., Hand, N., Seljak, U., et al. 2019, *Journal of Cosmology and Astroparticle Physics*, 010–010

Challinor, A. & Lewis, A. 2011a

Challinor, A. & Lewis, A. 2011b, *Phys. Rev. D*, 84, 043516

Chaussidon, E., Yèche, C., de Mattia, A., et al. 2025, *Journal of Cosmology and Astroparticle Physics*, 2025, 029

Chen, X. 2010, *Advances in Astronomy*, 2010

Chiarenza, S., Krolewski, A., Bonici, M., et al. 2025, Constraining primordial non-Gaussianity from DESI DR1 quasars and Planck PR4 CMB Lensing

Chudaykin, A., Ivanov, M. M., & Philcox, O. H. E. 2025, Reanalyzing DESI DR1: 3. Constraints on Inflation from Galaxy Power Spectra & Bispectra

Dalal, N., Doré, O., Huterer, D., & Shirokov, A. 2008, *Phys. Rev. D*, 77, 123514

D’Amico, G., Lewandowski, M., Senatore, L., & Zhang, P. 2023, Limits on primordial non-Gaussianities from BOSS galaxy-clustering data

Fabbian, G., Alonso, D., Storey-Fisher, K., & Cornish, T. 2025, Constraints on primordial non-Gaussianity from Quaia

Foreman-Mackey, D., Hogg, D. W., Lang, D., & Goodman, J. 2013, *Publications of the Astronomical Society of the Pacific*, 125, 306–312

Giannantonio, T., Scranton, R., Crittenden, R. G., et al. 2008, *Physical Review D*, 77

Gorski, K. M., Hivon, E., Banday, A. J., et al. 2005, *The Astrophysical Journal*, 622, 759–771

Grossi, M., Verde, L., Carbone, C., et al. 2009, *Monthly Notices of the Royal Astronomical Society*, 398, 321–332

Guédezounme, S. L., Jolicoeur, S., & Maartens, R. 2025, *Journal of Cosmology and Astroparticle Physics*, 2025, 063

Guth, A. H. 1981, *Phys. Rev. D*, 23, 347

Guth, A. H. & Pi, S.-Y. 1985, *Phys. Rev. D*, 32, 1899

Hernández-Monteagudo, C., Balaguera-Antolínez, A., von Marttens, R., et al. 2024, *arXiv e-prints*, arXiv:2412.14826

Hernández-Monteagudo, C., Ross, A. J., Cuesta, A., et al. 2014, *MNRAS*, 438, 1724

Hernández-Monteagudo, C., Chaves-Montero, J., & Angulo, R. E. 2020a, *Monthly Notices of the Royal Astronomical Society: Letters*, 503, L56–L61

Hernández-Monteagudo, C., Chaves-Montero, J., Angulo, R. E., & Aricò, G. 2020b, *Monthly Notices of the Royal Astronomical Society: Letters*, 503, L62

Hivon, E., Gorski, K. M., Netterfield, C. B., et al. 2002, *The Astrophysical Journal*, 567, 2–17

Komatsu, E. & Spergel, D. N. 2001, *Phys. Rev. D*, 63, 063002

Krolewski, A., Percival, W. J., Ferraro, S., et al. 2024, *Journal of Cosmology and Astroparticle Physics*, 2024, 021

Lang, D. 2014, *AJ*, 147, 108

Langlois, D. 2010, *Inflation and Cosmological Perturbations* (Springer Berlin Heidelberg), 1–57

Laurent, P., Eftekharzadeh, S., Goff, J.-M. L., et al. 2017, *Journal of Cosmology and Astroparticle Physics*, 2017, 017–017

Legrand, L., Hernández-Monteagudo, C., Douspis, M., Aghanim, N., & Angulo, R. E. 2021, *Astron. Astrophys.*, 646, A109

Lewis, A. & Challinor, A. 2011, *CAMB: Code for Anisotropies in the Microwave Background*, *Astrophysics Source Code Library*, record ascl:1102.026

Lima-Hernández, A., Hernández-Monteagudo, C., & Chaves-Montero, J. 2022, *Journal of Cosmology and Astroparticle Physics*, 2022, 038

Matarrese, S. & Verde, L. 2008, *The Astrophysical Journal*, 677, L77–L80

Mueller, E.-M., Rezaie, M., Percival, W. J., et al. 2021, *arXiv e-prints*, arXiv:2106.13725

Piccirilli, G., Fabbian, G., Alonso, D., et al. 2024, *Journal of Cosmology and Astroparticle Physics*, 2024, 012

Planck Collaboration et al. 2019, Planck 2018 results. IX. Constraints on primordial non-Gaussianity

Planck Collaboration et al. 2020, *Astron. Astrophys.*, 641, A6, [Erratum: *Astron. Astrophys.* 652, C4 (2021)]

Rezaie, M., Ross, A. J., Seo, H.-J., et al. 2024, *Monthly Notices of the Royal Astronomical Society*, 532, 1902–1928

Rezaie, M., Ross, A. J., Seo, H.-J., et al. 2021, *Monthly Notices of the Royal Astronomical Society*, 506, 3439–3454

Ross, A. J., Percival, W. J., Carnero, A., et al. 2012, *Monthly Notices of the Royal Astronomical Society*, 428, 1116–1127

Schlafly, E. F., Meisner, A. M., & Green, G. M. 2019, *The Astrophysical Journal Supplement Series*, 240, 30

Slosar, A., Hirata, C., Seljak, U., Ho, S., & Padmanabhan, N. 2008, *Journal of Cosmology and Astroparticle Physics*, 2008, 031

Starobinsky, A. 1980, *Physics Letters B*, 91, 99

Starobinsky, A. 1982, *Physics Letters B*, 117, 175

Storey-Fisher, K., Hogg, D. W., Rix, H.-W., et al. 2024, *The Astrophysical Journal*, 69

Takahashi, R., Sato, M., Nishimichi, T., Taruya, A., & Oguri, M. 2012, *The Astrophysical Journal*, 761, 152

Takahashi, T. 2014, *Progress of Theoretical and Experimental Physics*, 2014, 06B105

Vazquez Gonzalez, J. A., Padilla, L. E., & Matos, T. 2020, *Revista Mexicana de Física E*, 17, 73–91

Weaverdyck, N. & Huterer, D. 2021, *Monthly Notices of the Royal Astronomical Society*, 503, 5061

Appendix A: Investigating the reduced χ^2 behavior

The constraints reported in Tab. 2 show that the χ^2/dof values of the fit for the combined analysis of the four observables would result in a very low probability-to-exceed (PTE) value. We investigate here which data points drive this behavior and estimate again the constraints obtained by removing these data points to test the robustness of our joint measurement. In particular, we filter out the data points that are more than 2.5σ off with respect to the best-fit model. These are in total 6 data points, corresponding to the multipole bins centered at $\ell = 194.5$ for the C_ℓ^{kg} "Low-z" sample, $\ell = 30.5$ for the C_ℓ^{kg} "High-z" sample and $\ell = 12.5, 47.0, 194.5, 224.5$ for the C_ℓ^{kz} "Low-z" sample.

As already mentioned in Sec. 5, most of the tension with the best-fit model is coming from C_ℓ^{kz} data points; for instance, the χ^2/dof for this observable alone is 105/57 (see Tab. 2) and this is propagated to every combination including C_ℓ^{kg} . However, the constraining power of the CMB lensing - ARF cross-correlation for our datasets is quite limited and the final impact in the analysis of removing these data points is not significant. We list in Tab. A.1 the comparison between the baseline joint analysis and the case filtering the 6 data points that are $> 2.5\sigma$ off from the best-fit model. The results show full consistency with the baseline analysis and just a slight enlargement of the errorbars. For this case, the χ^2/dof is improved to 236/211, which corresponds to a PTE ~ 0.11 , just by removing 6 data points out of 220. This reflects that our results are robust enough despite the reported χ^2 values in Tab. 2 and motivates studies with more datasets to better understand the presence of systematic offsets in the cross-correlations with CMB lensing.

Data points	f_{NL}	b_0	α	χ^2/dof
Baseline	-3 ± 14	0.83 ± 0.06	0.37 ± 0.08	338/217
Filtered	3 ± 15	0.84 ± 0.07	0.34 ± 0.10	236/211

Table A.1. Median likelihood cosmological parameters with 1σ confidence intervals from the joint analysis of the four observables involved in our analysis, for the baseline case and the case removing data points in tension. We also list the χ^2 per degrees of freedom for each case.

Observable	f_{NL}	b_0	α
C_ℓ^{gg}	-8^{+38}_{-46}	1.30 ± 0.16	$-0.04^{+0.16}_{-0.15}$
C_ℓ^{zz}	-10^{+44}_{-51}	1.30 ± 0.16	$-0.03^{+0.17}_{-0.18}$
C_ℓ^{kg}	1 ± 23	$1.29^{+0.20}_{-0.16}$	$-0.03^{+0.16}_{-0.18}$
C_ℓ^{kz}	220^{+1279}_{-526}	$1.30^{+0.76}_{-0.36}$	$-0.61^{+0.50}_{-0.27}$
$C_\ell^{gg} + C_\ell^{kg}$	-1 ± 20	1.27 ± 0.10	-0.01 ± 0.09
$C_\ell^{zz} + C_\ell^{kz}$	0^{+34}_{-40}	$1.27^{+0.11}_{-0.10}$	$-0.02^{+0.12}_{-0.13}$
$C_\ell^{gg} + C_\ell^{kg} + C_\ell^{zz} + C_\ell^{kz}$	0 ± 14	1.26 ± 0.07	$-0.01^{+0.08}_{-0.07}$

Table B.1. Median likelihood cosmological parameters with 1σ confidence intervals for the baseline analysis from the four observables involved in our analysis and their combinations applied to Quaia mock data. The fiducial values of the parameters for the mocks are $f_{\text{NL}} = 0$, $b_0 = 1.26$ and $\alpha = 0$.

Appendix B: Constraints from Quaia mock data

In order to validate the MCMC inference pipeline and to provide a realistic estimation of the expected constraints on f_{NL} from the Quaia data and the improvement achieved with the addition of ARF, we calculate the constraints on the parameters for the four observables involved and their combinations using the average angular power spectra from our 1000 mock realizations. We list the results in Tab. B.1. Our mocks have as fiducial parameters $f_{\text{NL}} = 0$, $b_0 = 1.26$ and $\alpha = 0$. We recover these values with good agreement, and note that in particular for C_ℓ^{kz} alone the parameters are essentially unconstrained, as it happens for the real data. Regarding the final constraints achieved after the addition of ARF, we obtain a $\sim 30\%$ improvement on the f_{NL} errorbar. This reflects that the improvement that we report from the data is expected for a theoretical forecast of an ideal case without systematics, and that the $\sim 25\%$ improvement obtained with real data is not a product of tensions on the bias between observables, as already discussed within the text.